Comprehensive X-ray Structural Studies of the Quinolinate Phosphoribosyl Transferase (BNA6) from *Saccharomyces cerevisiae*‡

Eric di Luccio and David K. Wilson*

Section of Molecular and Cellular Biology, University of California, Davis, California 95616

Received October 11, 2007; Revised Manuscript Received January 28, 2008

ABSTRACT: Quinolinic acid phosphoribosyl transferase (QAPRTase, EC 2.4.2.19) is a 32 kDa enzyme encoded by the BNA6 gene in yeast and catalyzes the formation of nicotinate mononucleotide from quinolinate and 5-phosphoribosyl-1-pyrophosphate (PRPP). QAPRTase plays a key role in the tryptophan degradation pathway via kynurenine, leading to the *de novo* biosynthesis of NAD^+ and clearing the neurotoxin quinolinate. To improve our understanding of the specificity of the eukaryotic enzyme and the course of events associated with catalysis, we have determined the crystal structures of the apo and singly bound forms with the substrates quinolinate and PRPP. This reveals that the enzyme folds in a manner similar to that of various prokaryotic forms which are ~30% identical in sequence. In addition, the structure of the Michaelis complex is approximated by PRPP and the quinolinate analogue phthalate bound to the active site. These results allow insight into the kinetic mechanism of QAPRTase and provide an understanding of structural diversity in the active site of the *Saccharomyces cerevisiae* enzyme when compared to prokaryotic homologues.

Tryptophan catabolism is catalyzed by the six enzymes in the kynurenine pathway and is a major route for the *de novo* biosynthesis of nicotinate mononucleotide (NaMN),[1] a precursor of nicotinamide adenine dinucleotide (NAD^+). The majority of L-tryptophan in mammals is metabolized through this pathway with the remainder largely being converted to melatonin, serotonin, and other indoleamines (*1, 2*). NAD^+ has long been known as a ubiquitous cosubstrate used in redox reactions and energy metabolism by acting as a hydride acceptor. Since it is essential for so many reactions, organisms must maintain a constant NAD(H) reservoir. In higher eukaryotes, quinolinate phosphoribosyl transferase (QAPRTase, BNA6, EC 2.4.2.19) catalyzes the final step in the kynurenine pathway in *Saccharomyces cerevisiae* by catalyzing the transfer of quinolinate to 5-phosphoribosyl-1-pyrophosphate (PRPP) to yield NaMN, pyrophosphate, and carbon dioxide (Figure 1). QAPRTase provides the only known route for quinolinate metabolism and is a key enzyme involved in the regulation of the cellular concentrations of both quinolinate and tryptophan.

Quinolinate is a neurotoxic compound and is believed to be involved in a number of inflammatory neurological pathologies like Alzheimer's disease, AIDS-associated dementia, epilepsy, and Parkinson's disease, among others (*3*). As quinolinate is an endogenous agonist for the NMDA receptor, it inhibits uptake of glutamate into synaptic vesicles which leads to excessive glutamate concentrations and neurotoxicity (*4, 5*). Inappropriate activation of the NMDA receptor by quinolinate can lead to cell death from the high level of stimulation of sodium, potassium, and calcium channels (*6*). A reduction in the level of endogenous quinolinate biosynthesis could therefore limit the amount of brain damage in a number of various neurodegenerative conditions (*7*).

A number of medical conditions arise from improper regulation of quinolinate concentrations. Elevated levels of kynurenine and quinolinate have been found in eosinophilia-myalgia syndrome (*8*). Another mode of toxicity associated with high quinolinate concentrations is thought to arise from its ability to chelate Fe^{2+} which further reacts with hydrogen peroxide (H_2O_2) to produce the highly reactive hydroxyl radical and oxidized Fe^{3+} ion via the Fenton reaction (*9–11*). The hydroxyl radical is well-known to induce oxidative stress which is linked to an elevated *in vivo* concentration of quinolinate in neurodegenerative disorders such as Huntington's disease (*12*).

Catabolism via the kynurenine pathway is also critical in regulating cellular tryptophan concentrations. Low tryptophan levels are associated with inhibited T-cell responses, proliferation of viruses, protozoan parasites, and other pathogens in eukaryotic cells and also with a decreased rate of proliferation of tumor cells. In pregnant women, high tryptophan concentrations can lead to fetal immunotolerance problems (*13*). Much attention has been focused on the human indoleamine 2,3-dioxygenase (the yeast BNA2 homologue) which catalyzes the first and rate-limiting step in

‡ Data deposited as Protein Data Bank entries 3C2D, 3C2F, 3C2O, 3C2R, and 3C2V.

* To whom correspondence should be addressed: Section of Molecular and Cellular Biology, One Shields Ave., University of California, Davis, CA 95616. Phone: (530) 752-1136. Fax: (530) 752-3085. E-mail: dave@alanine.ucdavis.edu.

[1] Abbreviations: NAD^+, nicotinamide adenine dinucleotide; NaMN, nicotinate mononucleotide; PRPP, 5-phosphoribosyl-1-pyrophosphate; QAPRTase, quinolinate phosphoribosyl transferase; scQAPRTase, QAPRTase from *Saccharomyces cerevisiae* (BNA6); mtQAPRTase, QAPRTase from *Mycobacterium tuberculosis*; hpQAPRTase, QAPRTase from *Helicobacter pylori*; stQAPRTase, QAPRTase from *Salmonella typhimurium*; tmQAPRTase, QAPRTase from *Thermotoga maritima*; rmsd, root-mean-square deviation.

10.1021/bi7020475 CCC: $40.75
Published on Web 03/06/2008

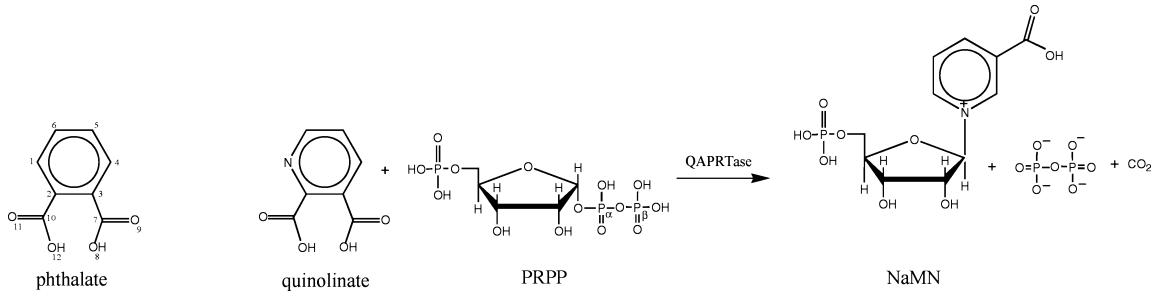

FIGURE 1: Schematic representation of the reaction catalyzed by the QAPRTase. The inhibitor phthalate, an analogue of quinolinate, is also shown.

this pathway (*2*). However, evidence suggests that QAPRTase is also important in controlling the flux of tryptophan through this pathway (*14*).

QAPRTase has been cited as a possible drug target in *Mycobacterium tuberculosis*, an organism that has little ability to salvage nicotinate and therefore depends on the *de novo* pathway (*15*). Inhibitors targeting this activity would therefore have to be specific and avoid inhibiting the human enzyme. Currently, no eukaryotic QAPRTase crystal structures have been reported. In this study, we describe the *S. cerevisiae* QAPRTase structure determined in apo, quinolinate-bound, PRPP-bound, and phthalate-bound forms. This sheds light on the kinetic and enzymatic mechanism of QAPRTase and also demonstrates structural differences at the quaternary level when compared to some of the prokaryotic forms.

MATERIALS AND METHODS

Cloning, Protein Expression, and Purification. The BNA6 gene (*YFR047C*) was PCR-amplified from *S. cerevisiae* genomic DNA using the 5′-primer GCTAGTGCATATGCCTGTTTATGAACACTTA and the 3′-primer ACTGCCCGGGATGAGCCAGTTTCAATGAGAA (*Nde*I and *Sma*I sites are underlined, respectively) and inserted into plasmid pTYB12 (New England Biolabs). The sequencing indicated no mutations were introduced by PCR. This was used to transform *Escherichia coli* expression strain BL21*, and recombinant scQAPRTase was expressed in LB medium containing 100 μg/mL ampicillin and induced with 500 μM isopropyl 1-thio-D-galactopyranoside for 12 h at 15 °C. Cells were harvested and lysed using a microfluidizer and then clarified by centrifugation. The resulting cell extracts containing wild-type BNA6 intein−chitin-binding domain fusion protein were passed over a column of chitin beads, which was washed with 20 column volumes of buffer A [20 mM Tris (pH 8.0), 500 mM NaCl, and 0.1 mM EDTA] supplemented with 0.1% Triton X-100 followed by 20 column volumes of buffer A alone. The QAPRTase−intein fusion protein was then cleaved on the chitin column by incubation for 12 h in buffer A with 50 mM 2-mercaptoethanol. QAPRTase was eluted in buffer A, dialyzed into 20 mM Tris (pH 8.0), and further purified by anion exchange chromatography on a quaternized polyethyleneimine HQ column using a BioCad Sprint system. A 0 to 3 M NaCl gradient was applied, and the protein eluted at a salt concentration of approximately 0.75 M. Purified QAPRTase was then exchanged into 20 mM HEPES (pH 7.4) with 20 mM NaCl and concentrated to 20 mg/mL using Millipore Ultrafree spin concentrators.

Analytical gel filtration experiments were carried out on a BioCad Sprint perfusion chromatography system (Perseptive Biosystems, Inc.) using a Superdex 200 HR 10/30 column (Amersham Pharmacia Biotech). The column was equilibrated with buffer containing 137 mM NaCl, 2.7 mM KCl, 4.3 mM Na_2HPO_4, and 1.4 mM KH_2PO_4 (pH 7.3). Purified QAPRTase was diluted to a concentration of 0.3 mg/mL in the same buffer and loaded onto the column. Elution was carried out at a flow rate of 0.5 mL/min. Protein elution was detected by absorbance at 280 nm. Calibration for molecular mass determination was carried out by using the following protein standards (Bio-Rad): thyroglobulin (670 kDa), γ-globulin (158 kDa), ovalbumin (44 kDa), myoglobin (17 kDa), and vitamin B_{12} (1.35 kDa).

Crystallization and Data Collection. Purified QAPRTase was crystallized at room temperature by the hanging drop vapor diffusion method. Drops containing 1 μL of protein solution (10–15 mg/mL) were mixed with 1 μL of the precipitant solution and suspended over a reservoir containing the precipitant solution [apoquinolinate, 20% PEG 3350 and 0.2 M ammonium formate; holoquinolinate, 20% PEG 3000 and 0.1 M citrate (pH 5.5); holo-PRPP, 20% PEG 3350 and 0.2 M ammonium chloride; holophthalate, 20% PEG 3350 and 0.2 M potassium formate; holophthalate-PRPP, 20% PEG 3350 and 0.2 M ammonium formate]. Crystals used in data collection were transferred to a cryoprotectant solution consisting of 70% (v/v) precipitant solution and 30% (v/v) ethylene glycol and flash-cooled in a stream of liquid nitrogen at 110 K. All QAPRTase cocrystals were obtained using stock protein incubated with either quinolinate, PRPP, phthalate, or PRPP and phthalate using a 20-fold excess of ligand. Both apo and holo crystals belonged to space group *R*32 ($\alpha = 90.00°$, $\beta = 90.00°$, and $\gamma = 120.00°$). There was one molecule per asymmetric unit except in QAPRTase holophthalate crystals where two molecules were found. The unit cell dimensions are as follows: $a = b = 154.9$ Å and $c = 68.9$ Å (apo); $a = b = 154.8$ Å and $c = 68.6$ Å (holoquinolinate); $a = b = 154.9$ Å and $c = 70.6$ Å (holo-PRPP); $a = b = 155.5$ Å and $c = 121.1$ Å (holophthalate); $a = b = 154.7$ Å and $c = 69.3$ Å (holophthalate-PRPP). All data sets were collected using beamline 9-2 at the Stanford Synchrotron Radiation Laboratory (SSRL) at 110 K using a MarMosaic-325 CCD detector (MarUSA Inc.) (Table 1). Data were reduced and scaled using MOSFLM and SCALA (*16–18*). Reflections with negative intensities were discarded. Before any refinement was performed, 5% (holo-BNA6) or 10% (apo-BNA6) of all the reflections were flagged for the calculation of an R_{free}.

Table 1: Data Collection and Refinement Statistics[a]

	apo	quinolinate	PRPP	phthalate	PRPP and phthalate
			Data Collection		
PDB entry	3C2D	3C2O	3C2F	3C2R	3C2V
wavelength (Å)	0.979126	0.88557	0.979397	0.97946	1.5418
resolution range (Å)	30–1.9 (1.97–1.90)	30–2.3 (2.36–2.3)	30–2.35 (2.43–2.35)	47–2.4 (2.46–2.4)	50–2.3 (2.38–2.3)
no. of unique observations	25007	14088	13619	22088	14205
total no. of observations	213024	155989	94569	239905	801341
completeness (%)	94.9 (72.5)	100 (100)	99.6 (97.0)	100 (100)	99.2 (98.4)
space group	*R*32	*R*32	*R*32	*R*32	*R*32
R_{sym}	0.064 (0.310)	0.094 (0.396)	0.068 (0.302)	0.099 (0.578)	0.083 (0.390)
$\langle I/\sigma(I)\rangle$	18.4 (3.0)	16.7 (5.4)	20.9 (5.1)	19.9 (4.1)	23.7(4.0)
			Refinement		
resolution range (Å)	28–1.9	29–2.3	29–2.35	47–2.4	44–2.3
no. of reflections used	20690	13215	12360	19371	12304
R_{cryst} (%)	22.3	20.0	21.1	18.8	22.4
R_{free} (%)	25.1	24.6	24.5	22.5	28.1
no. of protein, non-hydrogen atoms	2041	2040	2049	4083	2254
no. of non-protein atoms	250	115	130	231	198
rmsd for bond lengths (Å)	0.006	0.006	0.015	0.018	0.009
rmsd for bond angles (deg)	1.20	1.20	1.58	1.94	1.675
average main chain *B* value (Å^2)	44.77	51.28	45.43	50.70	50.58

[a] Values given in parentheses are for the high-resolution shell.

Phasing, Structure Determination, and Refinement. The initial phasing for apo-scQAPRTase came from a molecular replacement solution using PHASER and the QAPRTase structure from the *Salmonella typhimurium* structure (PDB entry 1QAP) as a search object (*19, 20*). The refined apo structure was then used to phase the remainder of the isomorphous data sets. Several rounds of crystallographic refinement and manual refitting using O, COOT, Refmac5, and CNS resulted in the final models of both apo- and holo-scQAPRTase (*21–23*). Flags on reflections used for the calculation of R_{free} were maintained throughout all refinements. Water molecules were automatically picked in COOT version 0.3 (MacOS X) and manually checked for appropriate hydrogen bonding and electron density agreement. The statistics associated with the final round of refinement are summarized in Table 1.

Structural overlays were done using SUPERPOSE and LSQKAB (CCP4 version 6.0.1 package) through CCP4i (MacOS X) (*24–26*). Accessible surface and volume calculations were carried out using both CNS version 1.1, areaimol (CCP4 package) with a solvent probe radius of 1.4 Å, and the Protein–protein Interaction Server (http://www.biochem.ucl.ac.uk/bsm/PP/server) (*23, 26, 27*).

Dynamic Light Scattering. Dynamic light scattering experiments were performed on a Protein Solutions DynaPro 99 molecular sizing instrument. The protein concentration was approximately 1 mg/mL in a buffer containing 10 mM Hepes (pH 7.4).

Fluorescence Measurements. Measurements of the fluorescence spectra were conducted on an Aminco-Bowman Series 2 luminescence spectrometer from SIM-Aminco Spectronic Instruments and were digitized using AB2 software version 5.0. Assays were conducted using 1.3 μM scQAPRTase (final concentration) in 10 mM KCl, 50 mM KH_2PO_4, and 0.5 mM EDTA (pH 7.0) at 25 °C with the exception of the PRPP/Mg^{2+} measurements which were conducted in 50 mM Tris and 6 mM $MgCl_2$ (pH 7.2). After the peak excitation and emission wavelengths had been determined, the emission scans were recorded between 300 and 350 nm at a rate of 150 nm/min with a continuous excitation wavelength of 280 nm (bandpass, 4 nm). Untransformed fluorescence data were plotted as a percentage change in the relative fluorescence intensity at peak emission λ_{max} (337 nm) versus substrate concentration. Assays with PRPP were conducted at a saturating level (8 mM) of phthalate. Kaleidagraph (Synergy Software Inc.) was used to fit appropriate equations to the data to determine binding parameters.

RESULTS AND DISCUSSION

Overall Structure. The quinolinate phosphoribosyl transferase (QAPRTase) structure from *S. cerevisiae* has been determined at 1.9 Å (apo), 2.3 Å (quinolinate-bound), 2.35 Å (PRPP-bound), 2.4 Å (phthalate-bound), and 2.0 Å (phthalate- and PRPP-bound) configurations using molecular replacement to phase the maps. The final model consists of residues 2−228, 250–261, and 268–295 of the 295 residues predicted with one molecule per asymmetric in the cases of the apo, quinolinate-bound, and PRPP-bound structures. The phthalate- and PRPP-bound and quinolinate-bound models contain identical residue ranges except they lack the C-terminal residue, residue 295. The phthalate-bound form had two molecules in the asymmetric unit.

The phosphoribosyl transferases (PRTases) consist of a large number of enzymes with varied substrate specificities and diverse amino acid sequences. The majority of PRTases are members of the "type I" family which contain a canonical PRPP binding motif with a five-stranded parallel β-sheet surrounded by α-helices (*28*). These include hypoxanthine-guanine phosphoribosyltransferase, adenine phosphoribosyltransferase, xanthine phosphoribosyltransferase, uracil phosphoribosyltransferase, orotate phosphoribosyltransferase, and glutamine PRPP amidotransferase (*28–34*).

The structure of scQAPRTase shows that it adopts a type II PRTase fold (Figure 2). Members of this family of enzymes exhibit a completely different topology containing a partial β/α-barrel and lack the conserved PRPP binding site found in the type I enzymes (*15, 20, 32*). Sequence homologies between QAPRTases and the nicotinic acid

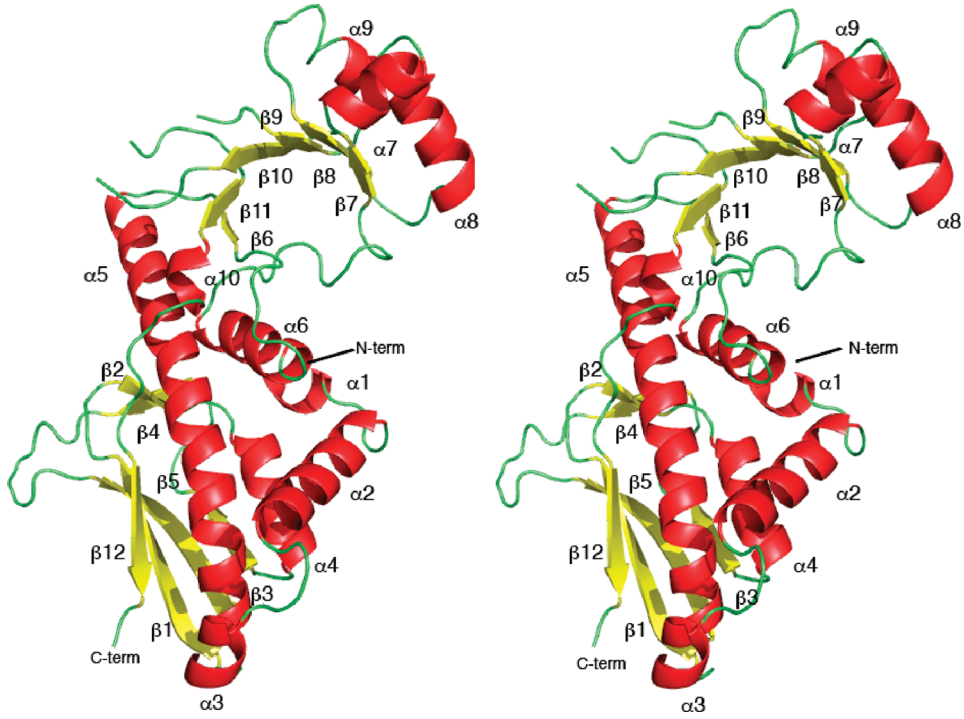

FIGURE 2: Stereoview of the main chain trace of scQAPRTase with α-helices colored red, *β*-strands yellow, and coils green. Secondary structural components are sequentially labeled.

Table 2: Comparison of the scQAPRTase Monomer, Dimer, and Hexamer with Other QAPRTase Structures[a]

		rmsd	pairwise % sequence similarity with scQAPRTase
hpQAPRTase (PDB entry 2B7N)	monomer	1.6 Å (253)	32
	dimer	1.7 Å (481)	
	hexamer	NSH	
mtQAPRTase (PDB entry 1QPR)	monomer	2.0 Å (245)	27
	dimer	2.0 Å (473)	
	hexamer	NSH	
stQAPRTase (PDB 1QAP)	monomer	1.5 Å (241)	30
	dimer	1.6 Å (479)	
tmQAPRTase (PDB entry 1O4U)	monomer	2.0 Å (233)	30
	dimer	2.5 Å (453)	

[a] The rmsd between α-carbons is shown with the number of residues compared in parentheses. In cases where rmsds were extremely high due to differences in trimerization of the dimers, no structural homology (NSH) is indicated. Note that stQAPRTase and tmQAPRTase do not form hexamers.

phosphoribosyltransfereases indicate they are currently the only members of the type II PRTase family (*15, 20, 35–37*). Structural similarity searches using the VAST server confirm this and identify the prokaryotic QAPRTases as the closest matches (Table 2) despite sharing a somewhat low level of sequence identity (~30%) (*15, 20, 37–40*). The anthranilate PRTases adopt a completely divergent fold and have been classified as type III (*41*).

The scQAPRTase monomer consists of two domains with an N-terminal domain composed of residues 2−124. This is composed of five helices (α1−α5) and five *β*-strands (*β*1−*β*5) and folds into an α/*β*-hammerhead type fold according to the SCOP classification (*42*). The C-terminal region of residues 135−295 folds into a broken *β*/α-barrel (or TIM barrel) domain made of five helices (α6−α10) and six *β*-strands (*β*6−*β*11) (*15, 37, 42*) (Figure 2). Typically, these domains require eight *β*/α-repeats to form a stable structure, but the empty volume left by the missing secondary structure is filled by a random coil between α6 and *β*7 (*43*). No electron density was found for the segments of residues 229–249 and 262–267 of scQAPRTase, predicted to be homologous to helices α8 and α9 of the QAPRTase from *M. tuberculosis* and helices H9 and H10 of the QAPRTase of *Thermotoga maritima*, respectively (*15, 37*).

Homodimeric Assembly. In all of the structures determined, a tightly associated scQAPRTase homodimer is observed (Figure 3A). This dimer is similar to that found in all known structures of prokaryotic QAPRTases (Table 2) (*20, 44, 45*). As with all *β*/α-barrel proteins, the active site is located at the C-terminal end of the inner *β*-barrel. It is also formed in part by the N-terminal domain of the second monomer (Figure 3A). An extensive hydrogen bond network and interactions involving 58 residues in each monomer stabilize the dimer and bury 2306 Å^2 per monomer at the interface. Similar large buried surfaces at the dimer interface (ranging from 2000 to 2700 Å^2) are found among other type II PRTases (*36, 37*). Dimerization is essential for activity because the active site of the enzyme is formed using residues from both of the molecules (described below). The missing segments of residues 229–249 and 262–267 are not predicted to be close to the active site center when using homologous structures as a guide (Figure 3B,C). The missing α-helix corresponding to the peptide of residues 229–249 is located at the periphery of the hexamer (Figure 3B). The segment of residues 262–267 is not part of the active site.

Hexameric Structure of scQAPRTase. QAPRTases from some species have been reported to be active in dimeric form, and others are hexameric. Dynamic light scattering analysis clearly indicates that the 32 kDa yeast QAPRTase forms a hexamer with a molecular mass of 191 kDa measured in

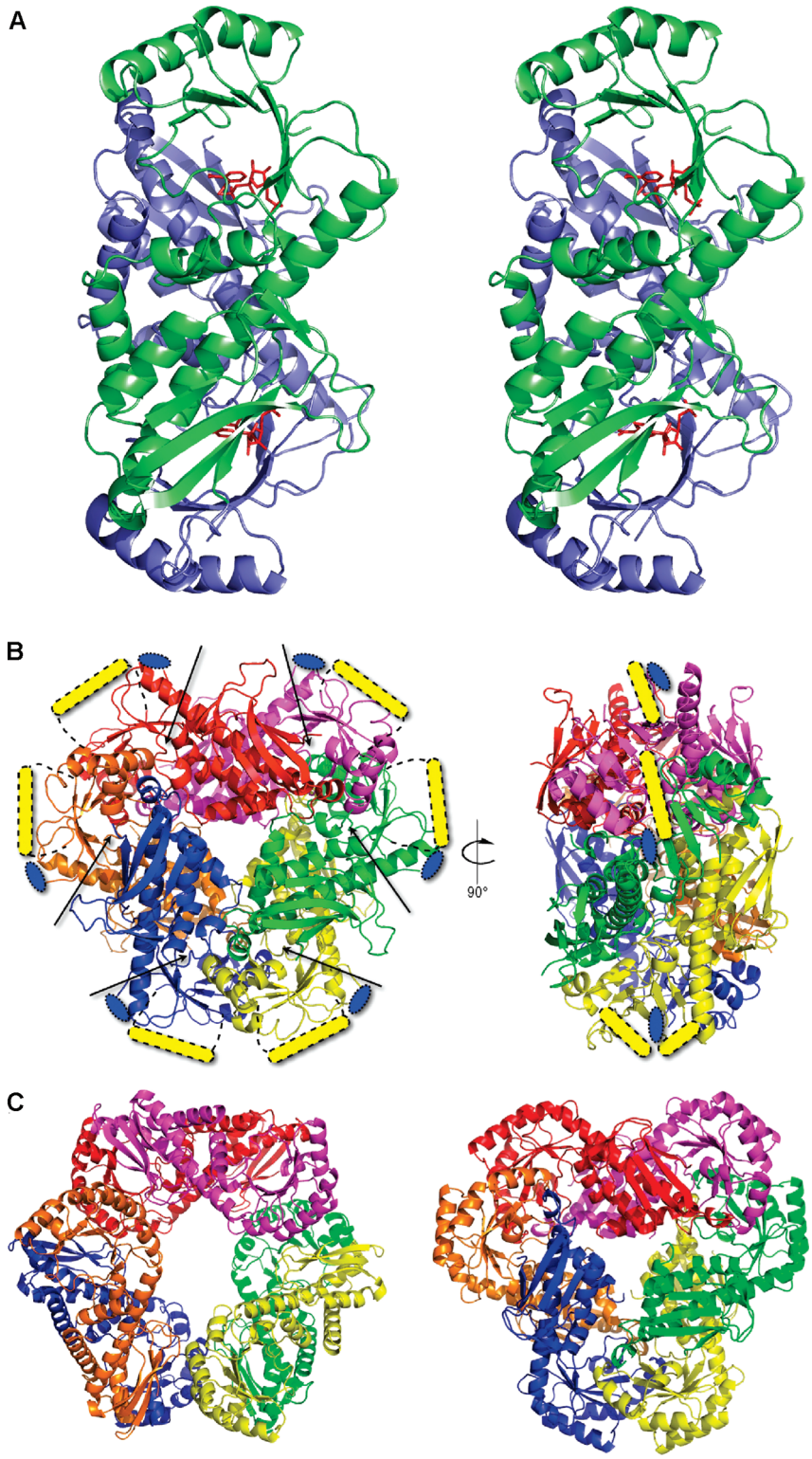

FIGURE 3: Oligomeric structures of QAPRTase. (A) Dimer of scQAPRTase complexed with phthalate and PRPP. (B) Hexamer of apo-scQAPRTase. Disordered regions not included in the model are sketched in yellow (residues 229–249) and blue (residues 262–267). Arrows indicate the general positions of the active sites. (C) Comparison with two other QAPRTase hexameric structures. scQAPRTase oligomerizes in a manner similar to that of *Helicobacter pylori* (right), while the *M. tuberculosis* form (left) has very similar dimers but completely different dimer–dimer interfaces.

solution. It is monodisperse and does not dissociate into either dimeric or monomeric forms even at low protein concentrations. This is consistent with the X-ray structure in which an identical hexamer is found in apo and all holo crystals despite some of them having different crystallographic parameters. The complex has an overall doughnut shape with a thickness of approximately 50 Å. The diameters of the outer ring and the inner empty ring are approximately 100 and 10 Å, respectively (Figure 3B). This overall structure is created by the 32 molecular symmetry (Figure 3B). Qualitatively, the scQAPRTase hexamer assembles in the same fashion as the *H. pylori* QAPRTase (hpQAPRTase) with helices α2−α4 of each scQAPRTase monomer facing toward the inside of the hexamer, exposing the active site region to the periphery

(Figure 3B,C) (*38*). A more detailed comparison of the oligomers reveals that the cant of the dimers is somewhat different and is associated with a tighter packing of the quaternary structure for scQAPRTase (see below). This produces a poorer structural alignment of the hexamers, although the dimers themselves remain structurally similar (Table 2). When one pair of dimers in each of the hexamers is overlaid, it leads to the offset of the two other dimers by a ~6° rotation along the lateral axis and ~4° along the longitudinal axis in the hexamer ring.

This mode of oligomerization is not the same throughout all of the type II PRTases. The *M. tuberculosis* enzyme (mtQAPRTase) has been reported to be a dimer (*15*) and a hexamer (*44*). Application of a noncrystallographic 3-fold symmetry axis to the dimer observed in this crystal structure creates a putative hexamer in the asymmetric unit (*15*). This assembly is arranged in a significantly different manner with the dimers being rotated 180° along the longitudinal axis when compared to either hpQAPRTase or scQAPRTase dimers (Figure 3C). The more distantly related nicotinate phosphoribosyl transferase from *Thermoplasma acidophilum* has been shown to be active as a hexamer (*36*). It oligomerizes in a manner similar to that seen in mtQAPRTase, emphasizing the relevance of this mode of oligomerization. The scQAPRTase hexamer is tightly packed with 64% of each monomer surface being buried as compared to 61% for hpQAPRTase and only 48% for mtQAPRTase, where the association is loose with a relatively large central pore (Figure 3B,C). QAPRTases from *Sa. typhimurium* and *T. maritima* do not form a hexamer in the crystal, and the former is known to be active as a dimer (*20*). Studies of QAPRTases from many higher eukaryotes indicate that hexamerization is a common theme (*46–48*). The association of scQAPRTase hexamers relies on extensive contacts which are primarily hydrophilic. Important hydrogen bonding interactions occur between the side chains or main chains of the Lys202/His250, His250/His250, Asn11/Gln65, Asn4/Gln65, Asp163/Phe199, Lys202/Phe199, Leu7/Asp30, Ala13/Ser23, and Arg151/Pro27 pairs. Examination of sequence conservation indicates that there is little or no correlation between amino acids at these positions and hexamerization, making it difficult to identify signature sequences which govern the mode of higher-order oligomerization.

Substrate Binding and Induced Conformational Changes. To investigate how the substrate binds to the active site, the structure of the enzyme was determined in complex with quinolinate, PRPP, and PRPP and phthalate (a quinolinate analogue). The structure of the quinolinate-bound form of the enzyme shows that it is inserted deeply in the active site pocket which is bordered by β-strands $\beta7-\beta11$. It is recognized by four direct hydrogen bonds involving Arg143, Arg166, and also Arg107 from the adjacent monomer in the homodimer which forms a basic pocket to complement the two carboxylates on the substrate (Figures 2 and 4A). Although enzymes frequently employ π-stacking to bind substrates of this nature, these types of interactions are notably absent in quinolinate binding. As such, the overall quinolinate ring orientation in the active site is dictated by the hydrogen bonding interactions with the carboxylate oxygens. There is also a water-mediated hydrogen bond between the carboxylate and Lys176. All of these residues are highly conserved in sequence and structure when compared to prokaryotic through mammalian homologues (Figure 5). There are no direct contacts with the quinolinate nitrogen, so there is no clear explanation for how or if the enzyme binds the substrate in a productive conformation with N1 directed toward the PRPP rather than C4 directed toward the PRPP. The rmsd between the apo and quinolinate-bound forms of the enzyme is only 0.27 Å which indicates that binding of the first substrate does not induce any significant global structural rearrangements.

The competitive inhibitor phthalate is structurally homologous to quinolinate, but the lack of a nitrogen atom in the aromatic ring prevents it from acting as a nucleophile and being a substrate for the enzyme. As expected, phthalate binds in a fashion that is virtually identical to that of quinolinate and is stabilized in the active site using the same hydrogen bond network (Figures 4B and 6A). The binding of phthalate does not induce any overall conformational changes when compared to the quinolinate bound with a Cα rmsd of overlaid structures of 0.43 Å (Figure 6A).

Although the enzyme follows a kinetically ordered mechanism with quinolinate binding first, PRPP can also bind in its absence to form a dead-end complex (*44*). The PRPP-bound structure shows that PRPP is held in place by eight direct hydrogen bonds with Lys144, Ser256, Gly257, Ser278, Arg107, and Leu291 from the adjacent monomer in the dimer (Figure 4C). There are also two water-mediated hydrogen bonds between the 5′-phosphate and Lys48 and the Leu291 backbone nitrogen of the adjacent monomer. Lys144 is particularly important for the binding since the PRPP is wrapped around its side chain which interacts with both phosphates at both the 1α and 5 positions. A comparable organization exists in the mtQAPRTase structure where the PRPP analogue 5-phosphoribosyl-1-(β-methylene)pyrophosphate (PRPCP) binds the same way in the active site and is similarly wrapped around Lys140 (*15*). In scQAPRTase, the binding of PRPP by itself does not induce any change in the active site or in the overall structure which remains virtually identical to the apo form with a Cα rmsd of 0.33 Å.

A comparison of the PRPP-bound and ternary structures reveals how the PRPP binding is changed by phthalate (and presumably quinolinate) binding (Figures 4C,D and 7). These all involve relatively subtle rearrangements confined to motions of the amino acid side chains since the overall rmsds between the structures are small (Figures 4C,D, 6A, and 7). The presence of phthalate in the active site creates new direct interactions with the PRPP between backbone atoms from Phe289 and Leu291 and phosphate 1β. Both Gly258 and Thr277 hydrogen bond with the 5′-phosphate. Lys144 engages in ionic interactions with phosphates at both the 5- and 1α-positions as well as O1 of ribose. Asp277 hydrogen bonds with O2 on the ribose and replaces Ser256. Gly257 and Lys48 are no longer involved in PRPP binding (Figures 4C,D and 7).

The ternary structure with both the inhibitor phthalate and PRPP shows that the coil region linking $\beta7$ and $\alpha7$ undergoes a spatial reorganization when compared to the apo form with main chain displacements of approximately 3 or 4 Å. In the phthalate- and quinolinate-bound structures, the Lys176 side chain engages in a water-mediated hydrogen bond with the carboxylate at the 3-position of quinolinate (Figure 4A,B). The conformational change in the loop induced by PRPP binding in the ternary complex causes the Lys176 side chain

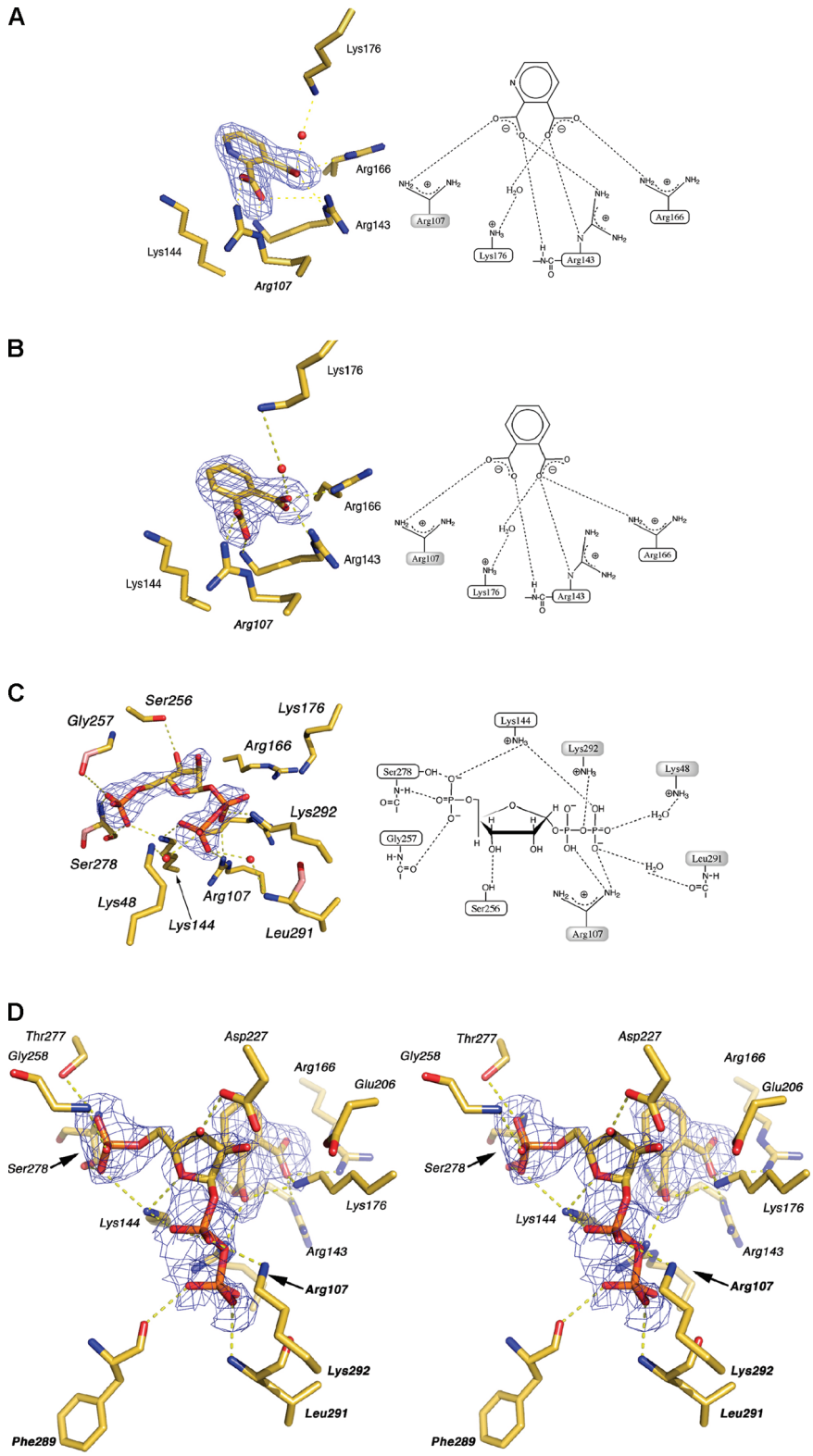

FIGURE 4: Active site details. $F_o - F_c$ omit electron density maps contoured at 3σ of binding site (left) and associated schematics of substrate binding (right) for (A) quinolinate, (B) phthalate, and (C) PRPP. A shaded residue in the schematics indicates that it is from another monomer. (D) Stereoview of the $F_o - F_c$ omit electron density maps contoured at 2σ of binding site phthalate and PRPP complexes. Residue names from the adjacent monomer in the dimer are shown in italic and bold.

to rotate, displacing the amine by 3.3 Å. It is then able to engage in hydrogen bonding with the carboxylate at the 2-position on the phthalate, losing the interaction with the carboxylate at the 3-position (Figures 4D and 6). When the binary and ternary forms are compared, PRPP binds in a somewhat different conformation. To accommodate the movement of Lys176, PRPP reorganizes around Lys144, but the phthalate remains at the same location when compared to the phthalate-bound binary structure (Figures 4D and 6A). The ribose is rotated approximately 20° away from the phthalate binding site as a result of the extra volume the phthalate occupies.

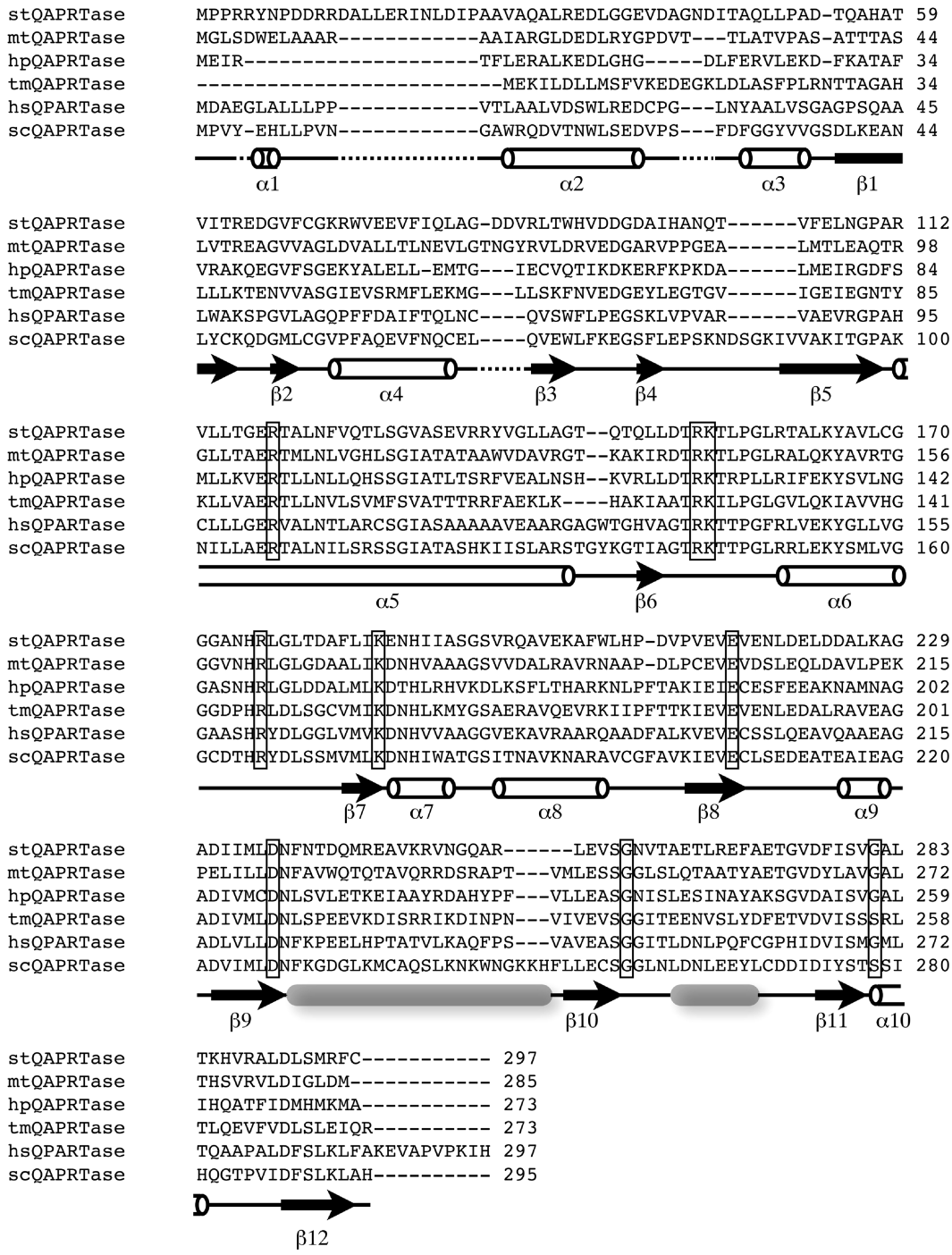

FIGURE 5: Sequence alignment of QAPRTases and the secondary structure for scQAPRTase. *Homo sapiens* denoted by hs. Residues involved in substrate binding in scQAPRTase are boxed, and the two disordered segments are colored gray.

When all scQAPRTase holo structures (quinolinate-bound, PRPP-bound, and PRPP- and phthalate-bound) are compared, a detailed kinetic mechanism can be sketched in which quinolinate remains static and PRPP undergoes conformational and positional changes during the various catalytic steps. In the ternary complex with both PRPP and phthalate, Lys144 anchors PRPP in the active site. The flexibility of Lys176 may permit it to interact with both substrates in the transient state, allowing it to play a crucial role in stabilizing the positions of the reactants.

Aside from the active site region, the binding of substrates does not induce significant overall conformational changes in the scQAPRTase monomer, dimer, or hexameric assembly when all structures are overlaid (rmsd $\leq$ 0.5 Å). The only significant change involves a movement of the flexible coil region linking β10 to β11 β-sheet which extends away from the active site with the binding of PRPP, or PRPP and phthalate.

Fluorescence Measurements of Dissociation Constants. To improve our understanding of substrate binding by QAPRTase, we used fluorescence measurements to determine the equilibrium dissociation constants of the substrates and the inhibitor phthalate (Table 3). In a previous study, Cao et al. (*44*) reported K_d values for stQAPRTase with substrates quinolinate (21 μM) and PRPP (53 μM). The substrate binding residues and the catalytic residues across the

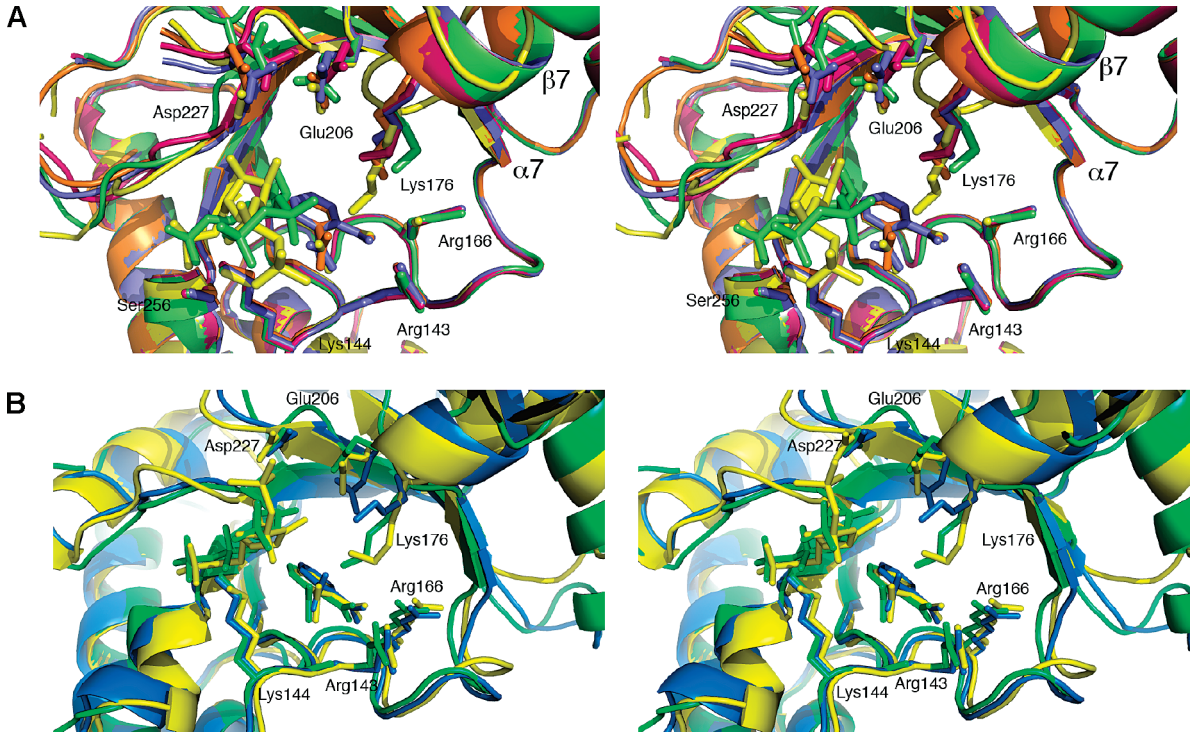

FIGURE 6: Structural comparison of QAPRTase active sites. (A) Overlay of the apo and holo structures (quinolinate, phthalate, PRPP, and phthalate and PRPP) showing the changes induced in the active site upon binding of various substrates and/or inhibitors: magenta for apo, light blue for quinolinate-bound, lime green for PRPP-bound, orange for phthalate-bound, and yellow for phthalate- and PRPP-bound. (B) Overlay of active sites. scQAPRTase and mtQAPRTase Michaelis complexes (with both PRPP and phthalate) along with hpQAPRTase phthalate-bound: green for scQAPRTase, yellow for mtQAPRTase, and blue for hpQAPRtase.

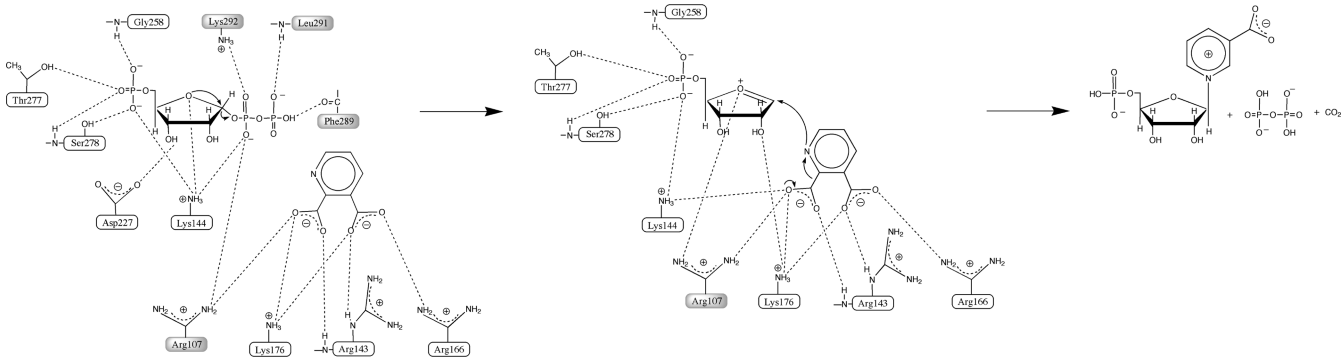

FIGURE 7: Schematic of substrate binding and proposed catalytic mechanism for scQAPRTase. The contacts shown in the ternary complex are derived from those observed in the PRPP- and phthalate-bound structure. A shaded residue in this schematic indicates that it is from another monomer.

Table 3: Dissociation Constants for Substrates and Phthalate Derived from Data Shown in Figure 1 of the Supporting Information[a]

substrate	dissociation constant (K_d) (mM)
quinolinate	0.45 ± 0.03
phthalate	0.78 ± 0.08
PRPP	10.1 ± 3.3
PRPP and 6 mM Mg^{2+}	4.6 ± 0.9

[a] PRPP binding was assessed at saturating phthalate concentrations. Addition of magnesium improved PRPP binding and also led to cooperative binding (n_H = 2.5).

QAPRTase family are highly conserved (Figure 5) which suggests that the substrates bind analogously in scQAPRTase and stQAPRTase, yet the dissociation constants are quite different. Furthermore, PRPP binding only in the presence of magnesium appeared to be cooperative with a Hill coefficient of 2.5. One possible explanation for the poorer substrate binding constants in scQAPRTase may be linked to an accessibility issue in the active site due to the tight packing of the dimers in the hexameric structure, whereas stQAPRTase exists only as a dimer in solution.

An increased PRPP concentration in the assays enhanced the fluorescence signal intensity as opposed to quinolinate or phthalate which quenched the signal. An enhancement of the fluorescence signal is most likely linked to an increase in the degree of shielding of tryptophans from the buffer. In scQAPRTase, Trp181 is the only residue which significantly switches environments in the Michaelis complex with both phthalate and PRPP bound. The side chain is located in the vicinity of the quinolinate binding site, moving within 16 Å of the quinolinate between the CH2 (Trp181) and O9 (phthalate) atoms in the binary complex. When both phthalate and PRPP bind, the Trp181 side chain rotates 180° away into a more hydrophobic pocket defined by residues Ile180, Leu175, Leu103, and Val35 from the adjacent monomer in

the dimer, decreasing the same distance to the tryptophan to 9 Å. In the binary complex, the Trp181 surface is 43% solvent accessible as opposed to the ternary complex, where it drops to 7%.

Catalytic and Kinetic Mechanism. In the scQAPRTase dimer, quinolinate or the inhibitor phthalate binds deeply at the bottom of the active site pocket and is almost completely buried with only 3% of the surface being solvent accessible. In the scQAPRTase−PRPP complex, PRPP is more exposed to the solvent with 16% of its surface remaining accessible. In the scQAPRTase ternary complex, PRPP binds adjacent to phthalate and becomes 9% surface accessible while phthalate is completely buried in the dimer. Similarly, in the mtQAPRTase ternary complex, phthalate is also totally buried and PRPCP is 8% solvent accessible. Cao et al. have shown that the reaction is ordered with quinolinate binding first followed by PRPP. As a consequence, the stQAPRTase−PRPP complex exists as a dead-end complex (*44*). This is consistent with observations made on the scQAPRTase−PRPP structure, where PRPP binds to the active site by itself and completely obstructs the entrance of the binding socket, making it impossible for quinolinate to bind afterward. On the basis of these structural observations, scQAPRTase appears to have an ordered kinetic mechanism similar to the one described for stQAPRTase (*44*).

Previous studies have shown that phosphoribosyl transferase reactions are likely to proceed via an S_N1 type reaction with an oxocarbenium intermediate (*15, 49–51*). Although the quinolinate is in a position where it could plausibly attack in an S_N2 mechanism, the orientation is not ideal. Furthermore, an S_N2 attack by the relatively bulky quinolinate is sterically difficult since C1 of ribose is not just a secondary carbon but is also torsionally constrained in a ring making it less accessible. The generation of the intermediate may require a general acid to induce cleavage of the pyrophosphate. On the basis of the structure, it is difficult to identify what fulfills this role. One possibility is Lys144, ordinarily a poor acid, which is the only residue which engages in a direct hydrogen bond with the phosphate at the α-position in the ternary complex with phthalate. Another alternative is a carboxylate from the quinolinate. A slight movement in the position of the quinolinate would allow this carboxylate, which is positioned only 4.6 Å from the nearest phosphate oxygen, to approach one of these oxygens at the α-position. It is unlikely that this is protonated, however, because of its proximity to the positive charges on the Arg107 and Lys176 side chains. Alternatively, since the pyrophosphate is a very good leaving group, there may be no need for the enzyme to activate it. The resulting oxocarbenium intermediate can be stabilized by the negatively charged region created by the phosphate at the 5-position and the liberated pyrophosphate. Further stabilization may occur through interactions with the carboxylate on the adjacent quinolinate. On the basis of the structure of the complex with phthalate and PRPP, the distance from the ribose ring oxygen and the nearest oxygen on the quinolinate is only 4.5 Å. This appears to be more plausible than the residues homologous to Glu206 and Asp227 fulfilling the role as proposed for mtQAPRTase (*15*). These residues are located on the opposite side of the sugar, adjacent to the 2- and 3-hydroxyls and positioned 7.3 Å (in the case of Glu206) and 5.6 Å (for Asp227), respectively, from O4 of ribose (Figure 4D). The reaction is completed through the attack of the nitrogen from the oriented quinolinate on the C1 position. Although the quinolinate is in a position where it could plausibly attack via an S_N2 mechanism, the orientation is not ideal. Furthermore, an S_N2 attack by the relatively bulky quinolinate is sterically very difficult since C1 of ribose is not just a secondary carbon but is also torsionally constrained in a ring making access more difficult.

Comparison with Other QAPRTases. QAPRTase has been proposed as a drug target against both *M. tuberculosis* and *H. pylori* and various other prokaryotes on the basis of its essential role in NAD^+ biosynthesis (*15, 20*). As such, inhibitors would have to exploit the structural differences arising from the level of sequence identity of 28% between the human and bacterial forms of the enzyme. Inhibitor specificity would appear to be exceptionally important given the known toxic effects of the substrate quinolinate on the brain and central nervous system.

Overall, the yeast enzyme is 43 and 27% identical to human and *M. tuberculosis* enzymes, respectively. Other structurally characterized QAPRTases are from *Sa. typhimurium* (30% identical to the yeast enzyme), *H. pylori* (32% identical), and *T. maritima* (30% identical) (Table 2). This sequence homology is reflected in structural similarity on the level of the monomer and dimer as well (Table 2), despite them sharing a low level of sequence identity. When overlaid with both spQAPRTase and hpQAPRTase, scQAPRTase substrate binding residues (Lys144, Lys176, Arg143, Arg166, Glu206, and Asp227) are structurally conserved and are similarly conserved in the pairwise sequence alignment (Figure 5). This is also reflected in the binding of substrates and product, where phthalate, quinolinate, and nicotinate mononucleotide bind identically as for BNA6 (Figure 6B).

The human QAPRTase shares the highest degree of sequence identity with the yeast enzyme, and all the catalytic residues are conserved with BNA6 and across all the QAPRTase families (Figure 5). The human enzyme is then likely to share the same active site and the same hexameric architecture as BNA6 as well as the same catalytic mechanism. These structural studies on the yeast QAPRTase therefore shed some light on the related human enzyme and provide useful and insightful data for further drug design.

ACKNOWLEDGMENT

Paul Donohoue is gratefully acknowledged for his help in protein expression and purification. Thanks are also due to Prof. Andrew Fisher for assistance with data collection.

SUPPORTING INFORMATION AVAILABLE

Binding curves for various scQAPRTase substrates and ligands (Figure S1). This material is available free of charge via the Internet at http://pubs.acs.org.

REFERENCES

1. Rongvaux, A., Andris, F., Van Gool, F., and Leo, O. (2003) Reconstructing eukaryotic NAD metabolism. *BioEssays 25*, 683–690.
2. Takikawa, O. (2005) Biochemical and medical aspects of the indoleamine 2,3-dioxygenase-initiated L-tryptophan metabolism. *Biochem. Biophys. Res. Commun. 338*, 12–19.
3. Guillemin, G. J., and Brew, B. J. (2002) Implications of the kynurenine pathway and quinolinic acid in Alzheimer's disease. *Redox Rep. 7*, 199–206.

4. Tavares, R. G., Tasca, C. I., Santos, C. E., Alves, L. B., Porciuncula, L. O., Emanuelli, T., and Souza, D. O. (2002) Quinolinic acid stimulates synaptosomal glutamate release and inhibits glutamate uptake into astrocytes. *Neurochem. Int. 40*, 621–627.
5. Tavares, R. G., Tasca, C. I., Santos, C. E., Wajner, M., Souza, D. O., and Dutra-Filho, C. S. (2000) Quinolinic acid inhibits glutamate uptake into synaptic vesicles from rat brain. *NeuroReport 11*, 249–253.
6. Stone, T. W. (1993) Neuropharmacology of quinolinic and kynurenic acids. *Pharmacol. Rev. 45*, 309–379.
7. Maharaj, H., Maharaj, D. S., and Daya, S. (2006) Acetylsalicylic acid and acetaminophen protect against oxidative neurotoxicity. *Metab. Brain Dis. 21*, 189–199.
8. Noakes, R., Spelman, L., and Williamson, R. (2006) Is the L-tryptophan metabolite quinolinic acid responsible for eosinophilic fasciitis? *Clin. Exp. Med. 6*, 60–64.
9. Platenik, J., Stopka, P., Vejrazka, M., and Stipek, S. (2001) Quinolinic acid-iron. (ii) complexes: Slow autoxidation, but enhanced hydroxyl radical production in the fenton reaction. *Free Radical Res. 34*, 445–459.
10. Muller, A. C., Dairam, A., Limson, J. L., and Daya, S. (2007) Mechanisms by which acyclovir reduces the oxidative neurotoxicity and biosynthesis of quinolinic acid. *Life Sci. 80*, 918–925.
11. Leipnitz, G., Schumacher, C., Scussiato, K., Dalcin, K. B., Wannmacher, C. M., Wyse, A. T., Dutra-Filho, C. S., Wajner, M., and Latini, A. (2005) Quinolinic acid reduces the antioxidant defenses in cerebral cortex of young rats. *Int. J. Dev. Neurosci. 23*, 695–701.
12. Ryu, J. K., Choi, H. B., and McLarnon, J. G. (2006) Combined minocycline plus pyruvate treatment enhances effects of each agent to inhibit inflammation, oxidative damage, and neuronal loss in an excitotoxic animal model of Huntington's disease. *Neuroscience 141*, 1835–1848.
13. Gonzalez-Hernandez, A., LeMaoult, J., Lopez, A., Alegre, E., Caumartin, J., Le Rond, S., Daouya, M., Moreau, P., and Carosella, E. D. (2005) Linking two immuno-suppressive molecules: Indoleamine 2,3 dioxygenase can modify HLA-G cell-surface expression. *Biol. Reprod. 73*, 571–578.
14. Shin, M., Ohnishi, M., Iguchi, S., Sano, K., and Umezawa, C. (1999) Peroxisome-proliferator regulates key enzymes of the tryptophan-NAD^+ pathway. *Toxicol. Appl. Pharmacol. 158*, 71–80.
15. Sharma, V., Grubmeyer, C., and Sacchettini, J. C. (1998) Crystal structure of quinolinic acid phosphoribosyltransferase from *Mycobacterium tuberculosis*: A potential TB drug target. *Structure 6*, 1587–1599.
16. Leslie, A. G. W. (1992) Recent changes to the MOSFLM package for processing film and image plate data. *Joint CCP4+ESF-EAMCB Newsletter on Protein Crystallography No. 26*, MRC Laboratory of Molecular Biology, Cambridge, U.K.
17. Evans, P. R. (1997) Scaling of MAD Data. *Proceedings of CCP4 Study Weekend on Recent Advances in Phasing*Daresbury Laboratory, Warrington, U.K.
18. Evans, P. R. (1993) Data reduction. *Proceedings of CCP4 Study Weekend Data Collection & Processing,* 114–122.
19. McCoy, A. J., Grosse-Kunstleve, R. W., Storoni, L. C., and Read, R. J. (2005) Likelihood-enhanced fast translation functions. *Acta Crystallogr. D61*, 458–464.
20. Eads, J. C., Ozturk, D., Wexler, T. B., Grubmeyer, C., and Sacchettini, J. C. (1997) A new function for a common fold: The crystal structure of quinolinic acid phosphoribosyltransferase. *Structure 5*, 47–58.
21. Emsley, P., and Cowtan, K. (2004) Coot: Model-building tools for molecular graphics. *Acta Crystallogr. D60*, 2126–2132.
22. Murshudov, G. N., Vagin, A. A., and Dodson, E. J. (1997) Refinement of macromolecular structures by the maximum-likelihood method. *Acta Crystallogr. D53*, 240–255.
23. Brunger, A. T., Adams, P. D., Clore, G. M., DeLano, W. L., Gros, P., Grosse-Kunstleve, R. W., Jiang, J. S., Kuszewski, J., Nilges, M., Pannu, N. S., Read, R. J., Rice, L. M., Simonson, T., and Warren, G. L. (1998) Crystallography & NMR system: A new software suite for macromolecular structure determination. *Acta Crystallogr. D54* (5), 905–921.
24. Krissinel, E., and Henrick, K. (2004) Secondary-structure matching (SSM), a new tool for fast protein structure alignment in three dimensions. *Acta Crystallogr. D60*, 2256–2268.
25. Kabsch, W. (1976) A solution for the best rotation to relate two sets of vectors. *Acta Crystallogr. A32*, 922–923.
26. Collaborative Computational Project Number 4 (1994) The CCP4 suite: Programs for protein crystallography. *Acta Crystallogr. D50*, 760–763.
27. Lee, B., and Richards, F. M. (1971) The interpretation of protein structures: Estimation of static accessibility. *J. Mol. Biol. 55*, 379–400.
28. Vos, S., de Jersey, J., and Martin, J. L. (1997) Crystal structure of *Escherichia coli* xanthine phosphoribosyltransferase. *Biochemistry 36*, 4125–4134.
29. Phillips, C. L., Ullman, B., Brennan, R. G., and Hill, C. P. (1999) Crystal structures of adenine phosphoribosyltransferase from *Leishmania donovani*. *EMBO J. 18*, 3533–3545.
30. Schumacher, M. A., Carter, D., Scott, D. M., Roos, D. S., Ullman, B., and Brennan, R. G. (1998) Crystal structures of *Toxoplasma gondii* uracil phosphoribosyltransferase reveal the atomic basis of pyrimidine discrimination and prodrug binding. *EMBO J. 17*, 3219–3232.
31. Scapin, G., Ozturk, D. H., Grubmeyer, C., and Sacchettini, J. C. (1995) The crystal structure of the orotate phosphoribosyltransferase complexed with orotate and α-D-5-phosphoribosyl-1-pyrophosphate. *Biochemistry 34*, 10744–10754.
32. Eads, J. C., Scapin, G., Xu, Y., Grubmeyer, C., and Sacchettini, J. C. (1994) The crystal structure of human hypoxanthine-guanine phosphoribosyltransferase with bound GMP. *Cell 78*, 325–334.
33. Schumacher, M. A., Carter, D., Ross, D. S., Ullman, B., and Brennan, R. G. (1996) Crystal structures of *Toxoplasma gondii* HGXPRTase reveal the catalytic role of a long flexible loop. *Nat. Struct. Biol. 3*, 881–887.
34. Muchmore, C. R., Krahn, J. M., Kim, J. H., Zalkin, H., and Smith, J. L. (1998) Crystal structure of glutamine phosphoribosylpyrophosphate amidotransferase from *Escherichia coli*. *Protein Sci. 7*, 39–51.
35. Chappie, J. S., Canaves, J. M., Han, G. W., Rife, C. L., Xu, Q., and Stevens, R. C. (2005) The structure of a eukaryotic nicotinic acid phosphoribosyltransferase reveals structural heterogeneity among type II PRTases. *Structure 13*, 1385–1396.
36. Shin, D. H., Oganesyan, N., Jancarik, J., Yokota, H., Kim, R., and Kim, S. H. (2005) Crystal structure of a nicotinate phosphoribosyltransferase from *Thermoplasma acidophilum*. *J. Biol. Chem. 280*, 18326–18335.
37. Schwarzenbacher, R., Jaroszewski, L., von Delft, F., Abdubek, P., Ambing, E., Biorac, T., Brinen, L. S., Canaves, J. M., Cambell, J., Chiu, H. J., Dai, X., Deacon, A. M., DiDonato, M., Elsliger, M. A., Eshagi, S., Floyd, R., Godzik, A., Grittini, C., Grzechnik, S. K., Hampton, E., Karlak, C., Klock, H. E., Koesema, E., Kovarik, J. S., Kreusch, A., Kuhn, P., Lesley, S. A., Levin, I., McMullan, D., McPhillips, T. M., Miller, M. D., Morse, A., Moy, K., Ouyang, J., Page, R., Quijano, K., Robb, A., Spraggon, G., Stevens, R. C., van den Bedem, H., Velasquez, J., Vincent, J., Wang, X., West, B., Wolf, G., Xu, Q., Hodgson, K. O., Wooley, J., and Wilson, I. A. (2004) Crystal structure of a type II quinolic acid phosphoribosyltransferase (TM1645) from *Thermotoga maritima* at 2.50 ÅA resolution. *Proteins 55*, 768–771.
38. Kim, M. K., Im, Y. J., Lee, J. H., and Eom, S. H. (2006) Crystal structure of quinolinic acid phosphoribosyltransferase from *Helicobacter pylori*. *Proteins 63*, 252–255.
39. Gibrat, J. F., Madej, T., and Bryant, S. H. (1996) Surprising similarities in structure comparison. *Curr. Opin. Struct. Biol. 6*, 377–385.
40. Madej, T., Gibrat, J. F., and Bryant, S. H. (1995) Threading a database of protein cores. *Proteins 23*, 356–369.
41. Mayans, O., Ivens, A., Nissen, L. J., Kirschner, K., and Wilmanns, M. (2002) Structural analysis of two enzymes catalysing reverse metabolic reactions implies common ancestry. *EMBO J. 21*, 3245–3254.
42. Murzin, A. G., Brenner, S. E., Hubbard, T., and Chothia, C. (1995) SCOP: A structural classification of proteins database for the investigation of sequences and structures. *J. Mol. Biol. 247*, 536–540.
43. Branden, C.-I. (1991) The TIM barrel: The most frequently occurring folding motif in proteins. *Curr. Opin. Struct. Biol. 1*, 978–983.
44. Cao, H., Pietrak, B. L., and Grubmeyer, C. (2002) Quinolinate phosphoribosyltransferase: Kinetic mechanism for a type II PRTase. *Biochemistry 41*, 3520–3528.
45. Kim, M. K., Kang, G. B., Song, W. K., and Eom, S. H. (2007) The Role of Phe181 in the Hexamerization of *Helicobacter pylori* Quinolinate Phosphoribosyltransferase. *Protein J. 26*, 517–521.

46. Okuno, E., White, R. J., and Schwarcz, R. (1988) Quinolinic acid phosphoribosyltransferase: Purification and partial characterization from human liver and brain. *J. Biochem. 103*, 1054–1059.
47. Iwai, K., and Taguchi, H. (1974) Purification and crystallization of quinolinate phosphoribosyltransferase from hog liver. *Biochem. Biophys. Res. Commun. 56*, 884–891.
48. Okuno, E., and Schwarcz, R. (1985) Purification of quinolinic acid phosphoribosyltransferase from rat liver and brain. *Biochim. Biophys. Acta 841*, 112–119.
49. Balendiran, G. K., Molina, J. A., Xu, Y., Torres-Martinez, J., Stevens, R., Focia, P. J., Eakin, A. E., Sacchettini, J. C., and Craig, S. P., III (1999) Ternary complex structure of human HGPRTase, PRPP, Mg^{2+}, and the inhibitor HPP reveals the involvement of the flexible loop in substrate binding. *Protein Sci. 8*, 1023–1031.
50. Schumacher, M. A., Bashor, C. J., Song, M. H., Otsu, K., Zhu, S., Parry, R. J., Ullman, B., and Brennan, R. G. (2002) The structural mechanism of GTP stabilized oligomerization and catalytic activation of the *Toxoplasma gondii* uracil phosphoribosyltransferase. *Proc. Natl. Acad. Sci. U.S.A. 99*, 78–83.
51. Sinha, S. C., and Smith, J. L. (2001) The PRT protein family. *Curr. Opin. Struct. Biol. 11*, 733–739.

BI7020475